

# Astronomical adaptive optics

## I. Modal control optimization

E. Gendron<sup>1,2</sup> and P. Léna<sup>1</sup>

<sup>1</sup> Observatoire de Paris et Université Paris VII, U.R.A. CNRS 264, F-92195 Meudon Cedex, France

<sup>2</sup> Laserdot, Route de Nozay, F-91460 Marcoussis, France

Received 15 March 1994 / Accepted 12 April 1994

**Abstract.** The value of adaptive optics (AO) for astronomy no longer needs to be demonstrated. To match the extreme requirements of astronomy in terms of resolution and sensitivity requires us to optimize an AO system to a great variety of situations. In particular, this paper addresses the case of low flux levels and shows that the final image quality can be improved by adapting the spatial and temporal correction performance of the AO system. The wavefront is considered as a weighted sum of spatial modes. Each mode has an individual behavior characterized by its signal to noise ratio and correlation time. Taking this into account leads us to attribute a specific, optimized correction bandwidth to each mode. To apply this optimization method to a practical use of adaptive optics, one proposes a scheme where all the required inputs are collected by the AO system itself. The method becomes entirely independent of theoretical assumptions about the turbulence.

**Key words:** atmospheric effects – methods: data analysis – telescopes – techniques: miscellaneous

### 1. Introduction

Recent developments have shown the application of adaptive optics (AO) to astronomical observation and its great potential for the use of large ground based telescopes as well as for multi-aperture interferometry (Léna 1994a; 1994b). A number of potential strategies remain open for discussion in the design of the most efficient instrument. While the unanimous goal is to compensate for the atmospheric turbulence and ultimately restore an image being diffraction limited or close to it, a number of parameters do restrict what can be practically achieved in terms of energy concentration in the diffraction limited core of the image: vertical and temporal structure of the atmospheric turbulence, magnitude of the reference source, wavelength of sensing and wavelength of observation, performance of the wavefront

sensor, isoplanatic field, etc. Some of these limitations may be relaxed by the prospect of using an artificial star as reference (Fugate et al. 1991; Primmerman et al. 1991), a possibility already demonstrated, but even then most of the considerations developed here still apply. In addition to these basic external parameters, some internal system parameters such as sampling frequency and time lag in the servo loop also influence the final image quality.

The perturbed wavefront over the pupil may be considered as the superposition of spatial modes with increasing spatial frequency and showing different temporal behaviour, while a correcting system is described by its number of degrees of freedom, ranging from a few (Roddier et al. 1991) to several hundred in systems developed for Defense applications (Fugate 1992).

It has been suggested (Léna 1990) to consider a strategy using a modal control of the AO system, where the latter is optimized for any given particular observation by an adjustment of its internal parameters: temporal response, number of corrected modes or others. The goal is to obtain the best image quality, measured with a criterium to be defined, using at best all the available information. In other words, the system is not only adaptive to the instantaneous state of the atmospheric turbulence, but its internal configuration is also adaptive to the particular observation being carried out. This modal control is an extensive concept already explored.

Most of the AO systems work in closed loop. They consist of a wavefront sensor, a real-time processor and one or several deformable mirrors. A control matrix defines the control voltages applied to the mirror. The goal is to optimize this matrix in terms of system characteristics and observing conditions. The optimization parameters may be determined from measurements made before closing the loop, as the turbulence may be non-stationary, and more generally the observing conditions may change with time. Although a number of articles deal with optimum reconstruction methods or matrices (Fried 1977; Southwell 1980; Wallner 1983) most of them address the open-loop case.

This paper discusses the theory in the closed loop case, focusing on the temporal aspects of the problem, and presents a

*Send offprint requests to:* E. Gendron

method of applying it to a real case. Section 2 gives the overview of modal control optimization. In Sect. 3, a physical approach and detailed analysis of an optimization scheme are given. Section 4 enumerates the parameters and instrumental constraints encountered in a practical case, namely an AO system installed on a telescope for astronomical observation. Section 5 describes the optimization behavior, as seen from the observer's point of view, i.e. in terms of parameters such as seeing conditions or wind velocity.

## 2. Modal control

This section recalls the overall components and general configuration of an AO system and defines some important concepts to be used later.

### 2.1. Vocabulary and notation

*Mirror controls* stands for the set of driving signals applied to the mirror.

The term *measurement* stands for the wave-front slope measurements, i.e. the set of the displacements of the spots of the Shack-Hartmann wavefront sensor (WFS).

*Modes* will be used to name any family of functions  $M_i(x, y)$  representing some spatial wave-front deformations over the pupil area. The *mirror modes* are a special case, described in Sect. 2.2.4.

Table 1 summarizes the notation.

### 2.2. The modes

#### 2.2.1. The perturbed wavefront

Neglecting scintillation (Roddier 1981), the instantaneous electric field amplitude is assumed to be constant over the pupil and is simply characterized by its phase  $\phi(x, y)$  defined over the pupil area. It is convenient to expand  $\phi$  on some basis of functions  $M_i(x, y)$  so that it can be written at any given time

$$\phi(x, y) = \sum_{i=1}^{\infty} z_i \cdot M_i(x, y) \quad (1)$$

The Zernike polynomials (Noll 1976) and the Karhunen-Loeve polynomials have been widely used for this purpose (Wang et al. 1978) but any other basis -orthonormal or not- of modes  $M_i$  may be of interest.

Then any incident wavefront becomes a vector  $\mathbf{z}$  whose components are  $z_1, \dots, z_{\infty}$ . The  $z_i$  are time-dependent variables. The vector  $\mathbf{z}$  belongs to a vector space  $\mathcal{E}$  of an infinite number of dimensions.

#### 2.2.2. The mirror

Let us assume a deformable mirror with  $a$  actuators corresponding to  $a$  degrees of freedom. These actuators can physically be distributed along the beam into several independent mirrors (for

**Table 1.** Notation

Quantity	Signification
$x, y$	cartesian coordinates in the pupil plane
$r, \theta$	polar coordinates in the pupil plane
$\phi(x, y)$	phase deformation
$\langle \dots \rangle$	time average value of ...
$\mathbf{u}$	vector $\mathbf{u}$ (bold character)
$u_i$	$i^{th}$ component of $\mathbf{u}$
$\mathcal{E}$	vector space of the functions defined over the pupil area
$\mathcal{M}$	"mirror space": see Sect. 2.2.4
$D$	interaction matrix between the mirror and the sensor
$D_{\infty}$	see 2.2.3
$D^+$	$(D^t D)^{-1} D^t$ , mode control matrix
$U^t$	transpose of a matrix $U$
$U^{-1}$	inverse of a matrix $U$
$\mathbf{u}^t$	transpose of a vector $\mathbf{u}$
$r_0(\lambda)$	Fried's parameter at wavelength $\lambda$
$q$	number of measurements on the WFS
$\mathbf{s}$	measurement vector from the WFS
$a$	number of degrees of freedom of the mirror
$a'$	dimension of the mirror space $\mathcal{M}$
$\mathbf{z}$	control vector of the modes
$\mathbf{n}$	noise vector on the centroid position
$\mathbf{m}$	noise vector on the mode coefficients
$\sigma_n^2$	variance (or spectrum level) of the noise on the centroid position
$p(i)$	propagation coefficient of the noise, from the WFS to the $i^{th}$ mode coefficient
$T_c$	sampling period
$h_{cor}$	rejection transfer function, called correction transfer function here
$H_{cor}$	$\ h_{cor}\ ^2$
$h_n$	transfer function between the noise input and the noise sent on the mirror mode controls
$H_n$	$\ h_n\ ^2$

example one or several deformable mirrors and a tip-tilt dedicated mirror). The wavefront phase variation induced by an actuator deformation under a given voltage is called the *actuator influence function*. It is important that the phase variations be linear in terms of the applied voltages. This assumption is usually well verified for existing mirrors when the amplitude is kept reasonably low (a few micrometers).

Hence, the set of the phase deformations the mirror can produce is composed of all the linear combinations of the actuator influence functions. It is a vector space, subspace of  $\mathcal{E}$ . Immediately a question arises, what is the dimension of this subspace. Owing  $a$  degrees of freedom, the dimension is  $a$  if the  $a$  basic influence functions are linearly independent. Although this may be true from a theoretical point of view, they may not be *sufficiently* independent in the practical case. A typical example of this situation occurs when the deformable mirror is able to produce a tilt, as does the tilt mirror.

Hence some redundant configurations may exist ; they reduce the dimension of the generated subspace, i.e. the actual number of degrees of freedom. The choice between the useful and the redundant modes is imposed by the system capability to produce them correctly or not. Finally, this leads us to choose a basis for the mirror subspace. It is essential to restrict the mirror controls to a set of modes corresponding to some basic vectors of the actual generated subspace in  $\mathcal{E}$ .

### 2.2.3. Limitations introduced by the sensor

The wavefront sensor is the element of the system that measures the perturbed wavefront. For simplicity the choice is made of a Shack-Hartmann type, composed of a lenslet array conjugated with a pupil plane and making images on a detector. The displacement of each spot is measured from a reference position corresponding to a plane wave. This displacement is proportional to the averaged phase gradient over the subaperture. This quantity is called the wavefront slope. The set of the  $q$  slopes can be written as a vector  $\mathbf{s}$  of dimension  $q$  forming the input vector to the system. An important condition is that  $\mathbf{s}$  be linear in terms of the incident wavefront. Then there exists a linear relation between  $\mathcal{E}$  and the vector space of  $\mathbf{s}$ . Let associate an interaction matrix  $D_\infty$  with this linear map so that  $D_\infty \cdot \mathbf{z} = \mathbf{s}$ . This matrix should theoretically have an infinite number of columns characterizing the sensor response to the basic vectors of  $\mathcal{E}$ .

The more practical, classical interaction matrix  $D$  is experimentally measured on the system itself and determines the relation between the mirror and the sensor. It characterizes the same linear map as  $D_\infty$ , but is restricted to the mirror control subspace. It will be used below to compute the control matrix (2.3.1).

A limitation introduced by the sensor is that some mirror deformations can produce a null or a very small response on the WFS because the sensor cannot detect them with a sufficient accuracy -a piston mode for example. The locution *invisible modes* will be used to refer to those modes. They correspond to the eigenvectors of  $(D^t \cdot D)$  having a zero eigenvalue, or very a small one in the practical case.

### 2.2.4. The mirror modes

The goal is to work in a mirror subspace free of redundant modes, and free of invisible modes. The useful set of mirror controls is the vector space  $\mathcal{M}$  which is a subspace of  $\mathcal{E}$ , generated by the mirror controls and excluding the redundant and invisible modes. The first step is to determine a basis containing no redundant vectors. The second step is to measure the interaction matrix  $D'$  between this basis and the sensor. Hence, the invisible modes can be extracted by computing the eigenvalues and eigenvectors of  $(D'^t \cdot D')$  (Boyer et al. 1990). The last step is to build a basis of the orthogonal complement of the subspace of the invisible modes, this complement being the mirror space  $\mathcal{M}$ . Its dimension will be called  $a'$ . The term *mirror modes* will be used for any basic vector set of this space. There exist an in-

finite number of such choices. Some examples are described by Gendron (1993).

## 2.3. The control matrix

### 2.3.1. Definition

From now on,  $D$  will refer to the interaction matrix between the mirror modes and the sensor. The mirror is controlled from the measurements by a relation  $\mathbf{z} = D^+ \cdot \mathbf{s}$  where  $D^+$  is called the control matrix. The control matrix can be found from the least-square solution minimizing  $\|\mathbf{s} - D \cdot \mathbf{z}\|$ , leading to the generalized inverse of  $D$

$$D^+ = (D^t \cdot D)^{-1} \cdot D^t \quad (2)$$

which can always be found here because  $D$  has full column rank, due to the suppression of the invisible modes (see 2.2.4). Note that this matrix ensures the minimization of the measurement norm, which is characteristic of a closed loop system.

### 2.3.2. The wave-front sensor noise

Due to the finite number of photons available for wavefront sensing, noise appears on the wavefront sensor measurements. It is convenient to define the noise as the error on the wavefront phase difference between the edges of the subaperture. Two noise regimes are usually distinguished: quantum noise and detector read-out noise. In the case of a Shack-Hartmann type sensor equipped with a photon noise limited detector, the noise expression (Rigaut 1992) is

$$\sigma_n^2(\text{rd}^2) = \frac{2\pi}{r_0^2(\lambda) \cdot N} \quad (3)$$

where  $N$  is the number of photoelectrons per frame and unit area. The noise is independent of the subaperture size. It becomes less simple in the case of a read-out noise limited detector and is given as

$$\sigma_n^2(\text{rd}^2) = \frac{16}{3} \left[ \frac{\sigma_e}{G_s n_s \epsilon^3} \right]^2 \quad (4)$$

in (Rousset et al. 1987), where  $\sigma_e$  is the electronic noise expressed as the number of equivalent photoelectrons,  $G_s$  the average value of the peak of the image,  $n_s$  the number of pixels in one direction used for centroiding,  $\epsilon$  the ratio between the spot diameter and the subaperture width.

In any case the noise has quite a number of interesting properties: it is additive, has a zero average and a flat temporal spectral density so that it can be fully characterized by its spectrum level or its variance; it is uncorrelated between two subapertures and between two orthogonal measurements in one subaperture. It will be assumed that the noise variance is the same for each subaperture.

### 2.3.3. Noise propagation through the control matrix

In order to evaluate the signal-to-noise ratio (SNR) characteristics of the modes it is convenient to introduce the noise propagation coefficients. They are defined as the ratio between the noise variance propagated through the control matrix and the input noise variance. Let  $\mathbf{m} = D^+ \mathbf{n}$ , where  $\mathbf{n}$  is the noise vector on the centroid position, and obeying the properties listed above. The covariance matrix  $\langle \mathbf{n} \mathbf{n}^t \rangle$  reduces to a diagonal matrix with  $\sigma_n^2$  on the diagonal, and this leads to the covariance matrix of  $\mathbf{m}$ :

$$\langle \mathbf{m} \mathbf{m}^t \rangle = D^+ \cdot \langle \mathbf{n} \mathbf{n}^t \rangle \cdot D^{+t} = \sigma_n^2 (D^+ \cdot D^{+t}) \quad (5)$$

Using Eq. (2) leads to

$$\langle \mathbf{m} \mathbf{m}^t \rangle = \sigma_n^2 (D^t \cdot D)^{-1} \quad (6)$$

Moreover, the variance of the  $i^{th}$  component of  $\mathbf{m}$  can be written as  $\langle m_i^2 \rangle = p(i) \cdot \sigma_n^2$ , where the searched coefficients  $p(i)$  are the diagonal terms of  $(D^t \cdot D)^{-1}$ :

$$p(i) = (D^t \cdot D)_{ii}^{-1} \quad (7)$$

Rigaut (1992) has derived an expression of the  $p(i)$  for the Zernike polynomials, when the number of subapertures tends towards infinity. In order to establish that the  $p(i)$  are nearly independent of the number of subapertures, the propagation coefficients have been computed for Shack-Hartmann sensors with various numbers of subapertures, from  $5 \times 5$  to  $15 \times 15$ . The coefficient  $p(i)$  converges very rapidly towards the theoretical limit when the number of subapertures increases. In fact, it reaches this limit as soon as the mode is sufficiently well sampled by the Shack-Hartmann grid. This condition of correct sampling must always be filled for the modes to be corrected.

In Sect. 3.1 the theoretical value for the noise propagation coefficients on the Zernike polynomials will be used. For the polynomials of the form  $Z_{k,p}(r, \theta) = P_k(r) \cdot \cos(p\theta)$ , Rigaut (1992) gives

$$\begin{cases} p_{k,p} = 0.295 (k+1)^{-2.05} & \text{if } k = p \\ p_{k,p} = 0.186 (k+1)^{-2.00} & \text{if } k \neq p \end{cases} \quad (8)$$

## 3. The optimization scheme

### 3.1. A physical approach

This section gives a heuristic justification of the possibility to optimize the modal control, derived from the actual physical constraints, and describes the resulting command.

When a faint star is used as reference, the noise may increase indefinitely. For a very faint star, it may still be possible to correct for the tip-tilt, while higher order modes of high spatial frequencies will be difficult to reconstruct because they are buried in the WFS noise. This nevertheless requires a careful analysis, since the noise is a decreasing function of the mode order, as shown in Eq. (8).

What really matters is the signal-to-noise ratio (SNR) for each mode,  $SNR_i$ . It can be computed for the Zernike modes

**Table 2.** Normalized signal to noise ratios of the Zernike polynomials

Zernike mode	$SNR_i$
tilt	1.0
defocus ( $Z_4$ )	0.191
astigmatism ( $Z_5$ )	0.119
coma ( $Z_7$ )	0.0906
sph. abb. ( $Z_{11}$ )	0.0561
$Z_{60}$ ( $10^{th}$ order)	0.0132

by using the Eq. (8) and the expression of their variance in the atmospheric turbulence derived by Noll (1976). The turbulent modal spectrum drops off faster than the noise modal spectrum, so that the SNRs decrease with the mode order. As an example, the SNR for some different Zernike polynomials are given in Table 2 with a tilt SNR normalized to unity.

In order to be efficient, the correction should only be applied to the modes known with a sufficient SNR. The variance over the pupil area of the phase residual error is chosen as the image quality criterium. The modes are orthogonal, and the total error is the sum of the errors on each mode. Assuming that it is possible to act on any polynomial independently of others, the best correction is obtained when the phase residual error is reduced to a minimum for each mode. A mode has to be corrected only if the correction brings an improvement, i.e. if the error on this mode after correction is smaller than without correction.

How to compute the residual error ? As demonstrated in Sect. 3.2 this error is mainly the sum of two terms: the first one is the remaining uncorrected phase left by the system due to the finite correction bandwidth, and the second represents the noise introduced in the loop. It may be noticed that both quantities are functions of the system bandwidth. The first term is a decreasing function tending towards 0, the second increases. It may then be that the sum reaches a minimum somewhere.

Hence the idea of modal filtering can be carried further: this is developed in Sect. 3.2, where a method to optimize the correction bandwidth for each mode is presented. This leads to an adaptive system, where the actual number of degrees of freedom is tuned in terms of the observing conditions. Open-loop WFS data taken on the reference source just before closing the loop are used to establish the latter and derive any parameter required for the optimization.

### 3.2. Loop description

The servo system works in closed loop, with a frequency transfer function  $h_{wfs}(f)$  for the wavefront sensor detector, and  $h_{sys}(f)$  for the system. A first order transfer function is assumed, including an integrator in the closed loop and a time delay between the measurement and the action corresponding to the WFS detector read-out time and the computation time. The actuator transfer function of the actuators is assumed to be perfect, equal to 1. The expressions of the two functions  $h_{sys}$  and  $h_{wfs}$  are  $h_{sys}(f) = e^{-2i\pi\tau \cdot f} / 2i\pi \cdot f$  and



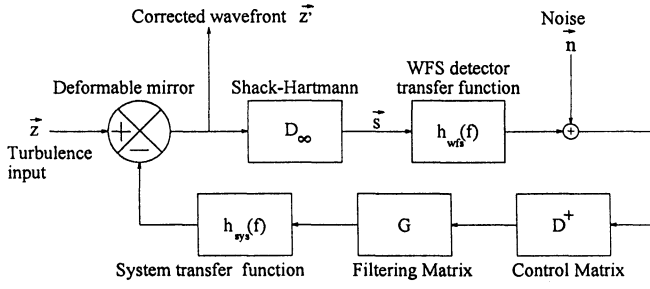


Fig. 1. Schematic representation of the control loop

$h_{wfs}(f) = \text{sinc}(\pi \cdot f \cdot T_e) \cdot e^{-i \cdot \pi \cdot \tau \cdot f}$ , where  $T_e$  is the sampling period and  $\tau$  the time delay. The open loop transfer function is then  $h_{ol}(f) = h_{wfs}(f) \cdot h_{sys}(f)$ .

In addition to the control matrix a diagonal filtering matrix  $G$  is applied. This means that the  $i^{th}$  mode reconstructed by  $D^+$  will be filtered by the  $i^{th}$  coefficient  $g_i$  of  $G$ . In a closed loop system, this coefficient directly controls the mode correction bandwidth.

The input turbulent wavefront is  $\mathbf{z}$ . It is a vector, as described in Sect. 2.2.1. The corrected wavefront is denoted  $\mathbf{z}'$ . The wavefronts  $\mathbf{z}$  or  $\mathbf{z}'$  are time-dependent variables. They should be written  $\mathbf{z}(t)$  or  $\mathbf{z}(f)$  if expressed in the Fourier space. However,  $\mathbf{z}$  will refer to them whatever the context, for the sake of brevity. The following equation can be derived from the loop figure:

$$\mathbf{z}' = \mathbf{z} - h_{ol}(f) \cdot G \cdot D^+ \cdot D_\infty \cdot \mathbf{z}' + h_{sys}(f) \cdot G \cdot D^+ \cdot \mathbf{n} \quad (9)$$

The columns corresponding to the mirror modes are identical in  $D$  and in  $D_\infty$ . Moreover, Eq. (2) leads to  $D^+ \cdot D = \text{Identity}$ . Hence the columns of  $D^+ \cdot D_\infty$  corresponding to the mirror modes form an identity matrix and any vector  $\mathbf{u}$  of the space  $\mathcal{M}$  obeys the relation

$$D^+ \cdot D_\infty \cdot \mathbf{u} = D^+ \cdot D \cdot \mathbf{u} = \mathbf{u} \quad (10)$$

This relation is false for  $\mathbf{u} \notin \mathcal{M}$ . Figure 2 makes this clearer.

Equation (10) allows us to invert Eq. (9) to find the corrected wavefront  $\mathbf{z}'$  as a function of the input turbulence, the noise, and the system characteristics.

$$\mathbf{z}' = \mathbf{z} - \frac{h_{ol}(f) \cdot G}{1 + h_{ol}(f) \cdot G} \cdot D^+ \cdot D_\infty \cdot \mathbf{z} - \frac{h_{sys}(f) \cdot G}{1 + h_{ol}(f) \cdot G} \cdot D^+ \cdot \mathbf{n} \quad (11)$$

The notation  $1$  stands for the identity matrix, and  $\frac{A}{B}$  stands for  $A \cdot B^{-1}$  when  $A$  and  $B$  are diagonal matrices. Let us define the matrix  $S$  as  $S = D^+ \cdot D_\infty$ , and express the  $i^{th}$  component  $z'_i$  of  $\mathbf{z}'$ .

$$z'_i = \frac{1}{1 + h_{ol}(f) \cdot g_i} z_i - \frac{h_{ol}(f) \cdot g_i}{1 + h_{ol}(f) \cdot g_i} \cdot \sum_{j=a'+1}^{\infty} S_{ij} \cdot z_j - \frac{h_{sys}(f) \cdot g_i}{1 + h_{ol}(f) \cdot g_i} \cdot \sum_{j=1}^p D_{ij}^+ \cdot n_j \quad (12)$$

The right hand side of Eq. (12) comprises three terms. The first one is the corrected mode, corresponding to the uncorrected

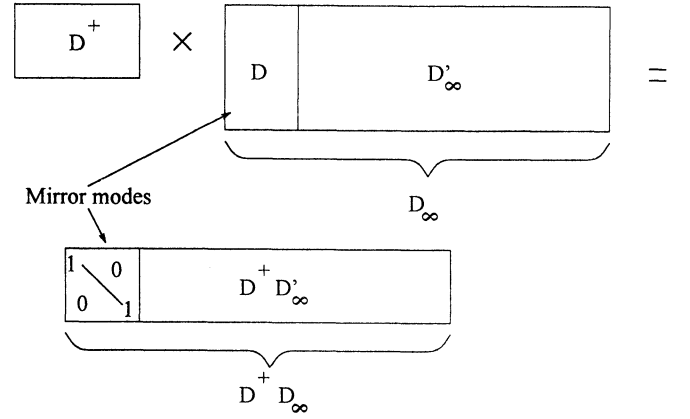


Fig. 2. Matrix product  $D^+ \cdot D_\infty$ . There is no cross-coupling between the mirror modes, each of them is perfectly identified by the system. This allows to control each mode separately

mode filtered by the rejection transfer function. The second term indicates the aliasing effects. It is only influenced by the modes orthogonal to the mirror subspace. The validity of the term ‘aliasing’ has already been discussed by Hermann (1981) or Southwell (1982). It is simply used here by analogy with the Fourier transform, to express that the modes of the orthogonal complement to the mirror space in  $\mathcal{E}$  (high spatial frequencies) may produce a response on the WFS (because of the incomplete WFS sampling), which will be interpreted by the system as mirror modes (lower frequencies). It is worth noticing that these errors are filtered by the closed loop transfer function.

Finally, the third term indicates the noise introduced in the system, which corresponds to the input noise propagated on the mode coefficient and filtered by a function nearly equal to the closed loop transfer function.

This equation demonstrates the possibility to modify the transfer function of a particular mode via  $g_i$ , without disturbing the other modes. It can easily be understood that under strong noise conditions the optimization will consist in tuning the gain - i.e. tuning the bandwidth - to reduce the induced noise and jointly the aliasing effect, to the detriment of the mode correction quality. The second term is usually small compared with the first, since the AO system is obviously designed to apply a useful correction. When the noise is important, the sum of the first poorly corrected term and the third term dominates in the equation compared with the aliasing term, whose importance is reduced by the noise optimization itself. It will consequently be assumed that the aliasing term of Eq. (12) can be neglected when working in a low flux regime. Then this equation can be rewritten

$$z'_i = h_{cor}(f, g_i) \cdot z_i - h_n(f, g_i) \sum_j D_{ij}^+ \cdot n_j \quad (13)$$

where  $h_{cor}$  is the rejection transfer function, i.e. the correction transfer function, and  $h_n$  the transfer function between the white noise in input and the noise actually sent to the active component. Since the noise is not correlated with the signal, the

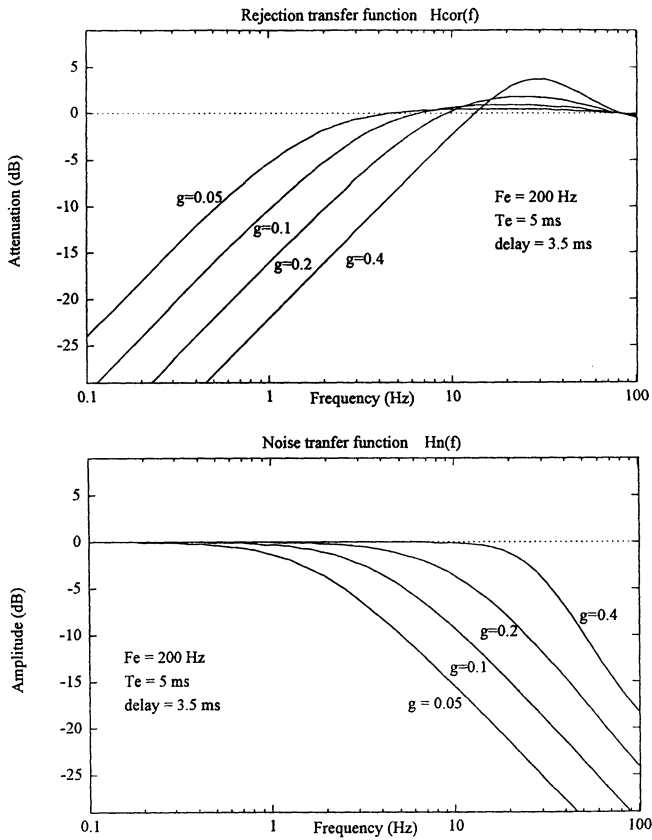


**Fig. 3.** Representation of the square modulus (expressed in decibels) of the functions  $H_{\text{cor}}$  and  $H_n$  in terms of the frequency (expressed in Hz), with the gain  $g$  as parameter. The loop includes a CCD, an integrator and a time delay. The conditions are a frame rate of  $F_e = 200$  Hz and a time delay of  $\tau = 3.5$  ms. The input turbulence power spectral density is multiplied by the function  $H_{\text{cor}}$  -usually called rejection transfer function- on output. The noise is multiplied by  $H_n$

variance of  $z'_i$  is

$$\begin{aligned} \langle z_i'^2 \rangle = & \int H_{\text{cor}}(f, g_i) \cdot \|z_i(f)\|^2 df \\ & + \int H_n(f, g_i) \cdot \|m_i(f)\|^2 df \end{aligned} \quad (14)$$

The functions  $H_{\text{cor}}$  and  $H_n$  stand for the squared modulus of  $h_{\text{cor}}$  and  $h_n$ , and  $m_i(f)$  is the noise on the mode  $i$ .

The quantitative behavior of  $H_{\text{cor}}$  and  $H_n$  versus the gain is illustrated by the simulation presented in Fig. 3.

#### 4. Practical implementation of the optimization

The previous section has shown that it is possible to minimize the residual phase errors on  $z'_i$  by a proper choice of the gain  $g_i$ . In Eq. (14),  $z'_i$  depends on the noise on the mode coefficient  $m_i$  and on the state of the atmosphere  $z_i$ . In principle, the optimization is possible when these quantities are properly known for a given observation. It is therefore appropriate to derive a method to estimate them in open loop before applying the correction, assuming they are constant over the time interval considered.

##### 4.1. Estimation of the noise

The problem is to evaluate the noise variance on the centroiding. Although some expressions of the noise variance have been derived (see 2.3.2), the actual regime of any real wavefront sensor is usually a superposition of quantum and read-out noise. In addition, let us enumerate some of the factors affecting the noise level above these fundamental noise sources: the application of a threshold on the sensor image, the spot widening by the intensifier point spread function, the intensifier gain dispersion, the observation of dissymmetrical extended objects, the sky background -changing with the proximity of the moon, or the object colour. This points to the need for a reliable, empirical method to directly measure the total noise.

The sensor gives a field of vectors measuring the phase gradient over the pupil aperture. Any function  $\phi$  verifies  $\text{rot}(\text{grad}(\phi)) = 0$ . Hence a field of vectors  $\mathbf{v}$  for which  $\text{rot}(\mathbf{v}) \neq 0$  is impossible to observe. Does this mean that some wavefront slope configurations cannot exist with a Shack-Hartmann? Unfortunately, due to the extended size of the subapertures, the microlenses average the phase gradient and make any arrangement of the field vector possible. Nevertheless, some configurations are generated by the turbulence with an infinitesimal probability. It is possible to find those special configurations by diagonalizing the theoretical covariance matrix  $\langle \mathbf{s} \cdot \mathbf{s}^t \rangle$  of the slope measurements  $\mathbf{s}$ . The correlation coefficients between two slopes can be computed with Eq. (24), presented in the Appendix. The diagonalization provides eigenvectors which are orthogonal and uncorrelated measurements. The eigenvalues indicate the variance of these configurations in the atmospheric turbulence. Hence the eigenvector associated with the lowest eigenvalue is the linear combination of the measurements for which the variance of the excitation by the turbulence is minimal. The basis change matrix  $B$  is the transpose of the matrix of the eigenvectors, for which  $B \cdot B^t = B^t \cdot B = \text{Identity}$ . Moreover,  $B \cdot B^t$  is also the noise propagation matrix, any  $p(i)$  is equal to 1; the eigenvalue is proportional to the SNR of the eigenvector.

Let examine a practical case of noise evaluation with a  $7 \times 7$  subapertures Shack-Hartmann. Figure 4 exhibits the last eigenvector corresponding to this Shack-Hartmann geometry, computed from Eq. (24). The following conditions are assumed: a telescope of 3.6 m diameter,  $r_o(\lambda) = 10$  cm at  $\lambda = 500$  nm, an overall atmosphere, telescope and system transmission of 0.3, a detector efficiency of 0.1 over a spectral range of 400 nm, a sampling rate of 200 Hz, and a quantum noise limitation allowing us to use Eq. (3) for a rough numerical estimate. To obtain a  $SNR_i$  of 1 on the eigenvector previously discussed, i.e. that associated with the lowest eigenvalue,  $\sigma_n^2$  leads to  $N = 1600$  photocounts per frame and per subaperture, corresponding to a magnitude  $m_v \approx 7.5$ . For example, if  $m'_v = 11$ , the atmospheric impact on the eigenvector becomes negligible compared to the WFS noise effect, hence the measurement of the eigenvector fluctuation variance leads to a noise estimate with a 4% accuracy, as deduced from  $m'_v - m_v$ .

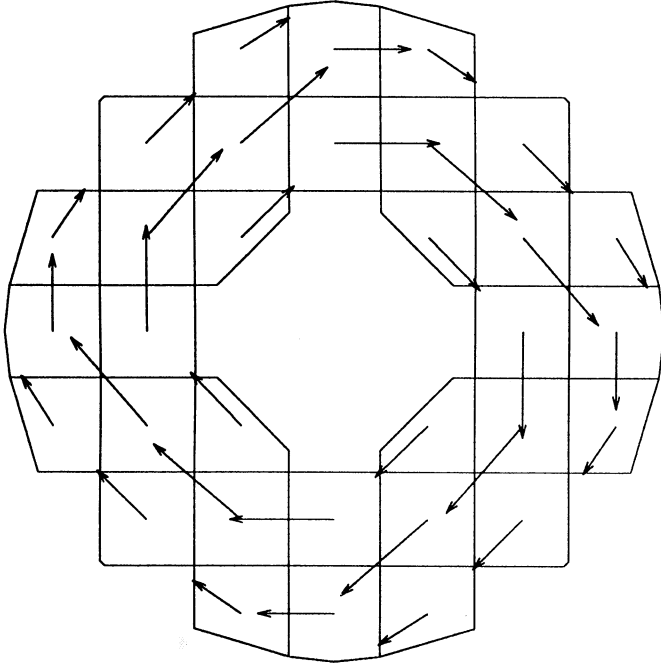


**Fig. 4.** Eigenvector of the covariance matrix of the slope measurements, associated with the smallest eigenvalue. The eigenvalue is proportional to the eigenvector SNR. For reference stars fainter than  $m_v \approx 10$  the SNR is so low that measuring the variance of this eigenvector in the atmospheric turbulence is equivalent to measuring the noise variance. Here the Shack-Hartmann has  $7 \times 7$  subapertures, and the central obstruction is 40% of the pupil diameter

The possibility to obtain a correct estimation of the noise level is hence demonstrated: in any case of noise regime (quantum noise, readout noise or other), it is simply deduced by measuring the variance of the fluctuations of the last eigenvector on a sequence of uncorrected wavefront slopes recorded on the reference object.

## 4.2. Estimation of the residual error

### 4.2.1. The residual error

The function  $H_{\text{cor}}(f, g)$  and  $H_n(f, g)$  only depend on the system characteristics: they can be measured or computed from a theoretical model. The term  $p(i)$  is deduced from the control matrix. By recording a temporal sequence of uncorrected wavefront slopes from the Shack-Hartmann data before closing the loop, it is possible to deduce the noise  $\sigma_n^2$ . It is also possible to reconstruct the temporal evolution of the mode coefficients, simply by multiplying by the control matrix  $D^+$ . The temporal evolution of each mode is obtained, and a Fast Fourier Transform provides  $\|\hat{z}_i(f)\|^2$ . This quantity is the sum of the mode power spectrum density  $\|z_i(f)\|^2$  and the noise  $\|m_i(f)\|^2$ , being both still unknown.

Due to the strong decrease of the turbulent spectrum at high frequencies, it is hopeless to fit the actual spectrum value under the noise, as it is hopeless to estimate the real noise at low

frequencies where turbulent effects dominate (Fig. 5). The positive counterpart of this negative point is that the high frequency part of the turbulent spectrum shape being under the noise, it has no weight in the value of  $\langle z_i^2 \rangle$ . In the same way, the low frequency noise also only has a weak impact on it, since turbulence dominates. Hence Eq. (14) can be rewritten:

$$\langle z_i^2 \rangle = \int H_{\text{cor}}(f, g_i) \cdot (\|\hat{z}_i(f)\|^2 - p(i) \cdot \sigma_n^2) df + p(i) \cdot \sigma_n^2 \cdot \int H_n(f, g_i) df \quad (15)$$

where each term is known. The only difference from Eq. (14) is that the random noise power spectral density has been replaced by a constant function with the appropriate amplitude  $p(i) \cdot \sigma_n^2$ .

The reason why  $\langle z_i^2 \rangle$  can be rewritten is not because the function  $\|\hat{z}_i(f)\|^2 - p(i) \cdot \sigma_n^2$  is an estimate of  $\|z_i\|^2$ : this assumption would be false. However, the *integrals* are very close to each other; this will be shown by computing the difference  $\delta$  between the true value (Eq. (14)) and this approximation (Eq. (15)).

### 4.2.2. Uncertainty on the estimate of the residual error

Making the assumption that the functions are known at some  $K$  discrete frequency samples  $f_k$ , the notations will be simplified:  $m_k$  stands now for the noise power spectral density at the  $k^{\text{th}}$  frequency sample  $f_k$ .  $H_{\text{cor}_k}$  and  $H_{n_k}$  are the values of the square modulus of the transfer functions at the same point. The average of the  $m_k$  is the noise variance  $p(i) \cdot \sigma_n^2$ , and the variance around this average value is  $p^2(i) \cdot \sigma_n^4$ . The quantity to evaluate is the difference between Eq. (14) and Eq. (15). Computing the mean square value gives

$$\delta^2 = \left\langle \left( \frac{1}{K} \sum_k (H_{\text{cor}_k} - H_{n_k}) \cdot (m_k - p(i) \cdot \sigma_n^2) \right)^2 \right\rangle \quad (16)$$

Since the  $m_k$  are not correlated, the expression becomes

$$\delta = \frac{p(i) \cdot \sigma_n^2}{K} \sqrt{\sum_k (H_{\text{cor}_k} - H_{n_k})^2} \quad (17)$$

Moreover, the functions  $H_{\text{cor}}$  and  $H_n$  always vary in an opposite way (Fig. 3): one equals 1 when the other is close to 0 and vice versa. This allows us to simplify Eq. (17), assuming that  $(H_{\text{cor}_k} - H_{n_k})^2 \approx 1$ . It gives

$$\delta = \frac{p(i) \cdot \sigma_n^2}{\sqrt{K}} \quad (18)$$

This expression shows that the uncertainty is independent of the gain  $g_i$ , and that the error can be lowered by increasing the number of points. A sampling frequency of 200 Hz and 10 seconds of turbulence recording provide  $K = 1000$  points for the power spectrum estimate. This gives an error standard deviation about 30 times lower than the noise level.

#### 4.3. Error minimization

Hence comes the gain optimization: the residual error can be computed from Eq. (15). In order now to optimize the gains, it is more convenient to differentiate Eq. (15) with respect to  $g_i$  under the integrals and to solve the equation:

$$\frac{d \langle z_i^2 \rangle}{dg_i} = 0 = \int \frac{dH_{\text{cor}}}{dg_i} \cdot [\|\hat{z}_i\|^2 - p(i) \cdot \sigma_n^2] df + p(i) \cdot \sigma_n^2 \cdot \int \frac{dH_n}{dg_i} df \quad (19)$$

The quantities  $\frac{dH}{dg}$  can be computed analytically, although they take a rather complex expression.

Solving Eq. (19) can be done by any method, for example the zero can be searched by dichotomy between two limits  $g_i = 0$  and the maximum  $g_i$  ensuring loop stability (2.3 dB maxi. for the closed loop transfer function). The following section puts this method into practice.

#### 4.4. Simulations

In order to illustrate the validity of the above approach, simulated cases are presented here. The atmospheric behavior often departs from a perfect Kolmogorov spectrum with infinite outer scale and full stationarity. As a matter of fact, numerous observations carried out with a particular system (the Come-On-Plus AO system, Rousset et al. 1993) give realistic inputs for the behavior of  $z_i$ . This will be treated in great detail in a forthcoming paper. Here the approach is restricted to a simple, ideal analytic description of the atmosphere.

##### 4.4.1. Atmospheric model

A theoretical curve made of two power laws will be used for the mode fluctuation power spectra. The theoretical shapes are in  $f^{-2/3}$  and  $f^{-11/3}$  respectively at low and high frequencies. The limit between the two domains is set by the cutoff frequency  $f_c$ . There exist a number of simulations and theoretical explanations, or measurements of the power spectral density of the fluctuations of the modes (Clifford 1971 ; Hogge et al. 1976 ; Greenwood et al. 1976 ; Greenwood 1978 ; Fields 1983 ; Acton et al. 1992 ; Madec et al. 1992 ; Roddier et al. 1993). They do not always agree on the basic phenomenon. While some (Madec et al. 1992 ; Roddier et al. 1993) agree on a *theoretical* high-frequency behavior in  $f^{-17/3}$ , the most common values usually found are in  $f^{-8/3}$  to  $f^{-11/3}$ . As stated in Greenwood (1978), “the spectral density could be almost anything”, since it depends on the wind velocity distribution along the  $C_n^2$  profile. Then, the choice of spectra in  $f^{-2/3}$  and  $f^{-11/3}$  for low and high frequencies respectively, although somewhat arbitrary, may represent a good compromise among what can usually be measured at various sites. Figure 5 shows a simulation of the temporal spectrum of a particular mode (astigmatism) under 0.83'' seeing conditions with a noise variance corresponding approximately to a flux of 6 photocount  $\text{m}^{-2} \text{frame}^{-1}$  with a quantum noise limited detector.

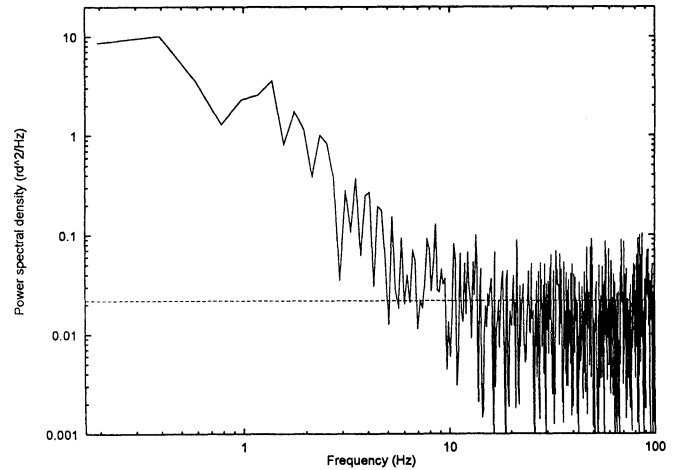


**Fig. 5.** Simulated spectrum of the astigmatism mode fluctuations, with  $f^{-2/3}$  and  $f^{-11/3}$  power laws, and a cutoff frequency of 1 Hz. The variance corresponds to a  $r_0$  of 12 cm on a 4 m telescope. Units are  $\text{rd}^2 \text{Hz}^{-1}$  at 500 nm. The noise variance is  $2.2 \text{ rd}^2 \text{Hz}^{-1}$ , corresponding to a flux level of 6 photocounts  $\text{m}^{-2} \text{frame}^{-1}$  with a quantum noise limited detector

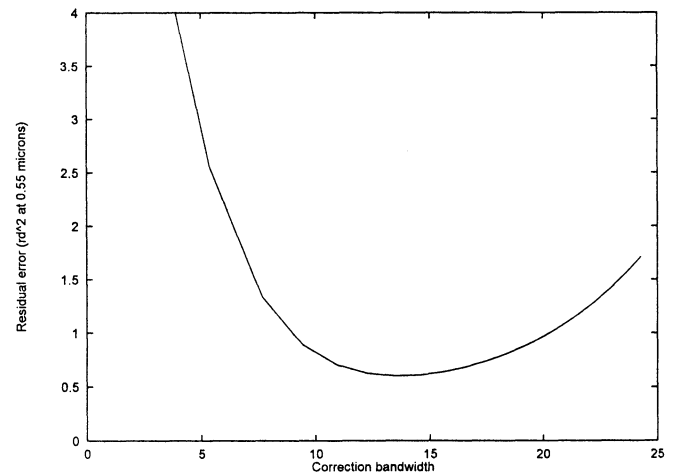
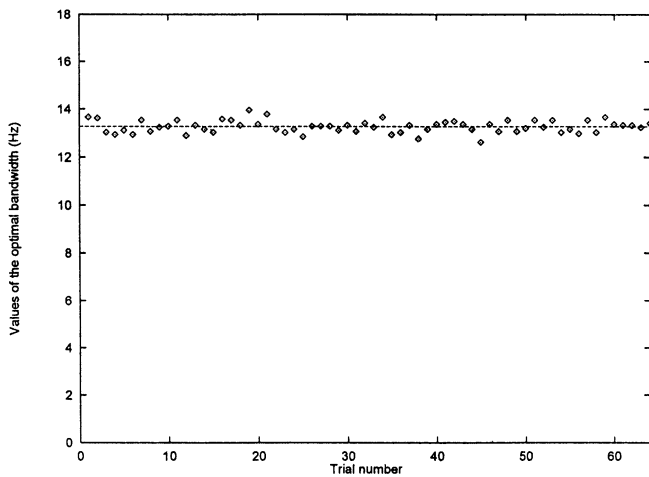


**Fig. 6.** Astigmatism residual phase error, expressed in  $\text{rd}^2$  at 500 nm in terms of the correction bandwidth. The closed loop conditions are a 200 Hz sampling frequency, 2 ms time delay, an integrator in the loop. The noise variance is  $2.2 \text{ rd}^2$ , corresponding to a flux level of 6 photocounts  $\text{m}^{-2} \text{frame}^{-1}$  with a quantum noise limited detector

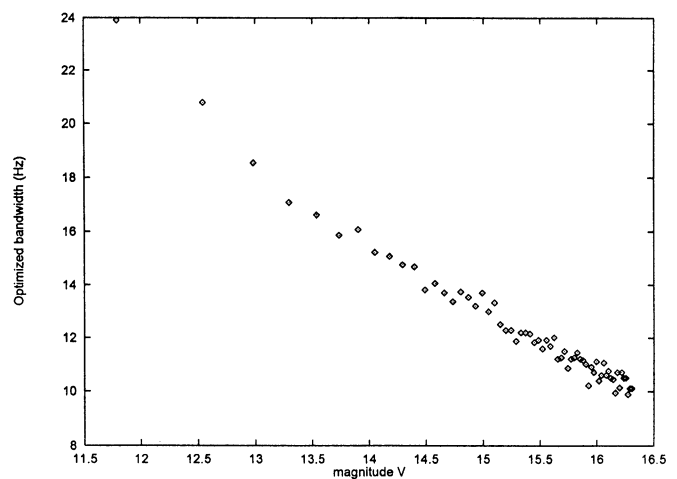
##### 4.4.2. Results

Figure 6 shows the result  $\langle z_i^2 \rangle$  of Eq. (15) in terms of the correction bandwidth, applied to the data shown on Fig. 5. The closed loop conditions are detailed in the caption of Fig. 6. It clearly demonstrates the need for an optimization: a gain of a factor 2 on the residual error appears between the maximum (25 Hz) and the optimum bandwidth where the minimum of the error is reached, around 14 Hz (the correction bandwidths are given at 0 dB for the rejection transfer function). This optimum is very close to the intersection between the turbulent spectrum and the noise level.





**Fig. 7.** Values of the optimized bandwidth in the same conditions as for the previous figure. The various values have been computed for some different noise realisations. The horizontal line indicates the averaged value



**Fig. 9.** Values of the optimized bandwidth in terms of the reference object magnitude. The input turbulence is a simulated spectrum of the Zernike astigmatism mode ( $n = 2$ ,  $m = 2$ ) fluctuations, with  $f^{-2/3}$  and  $f^{-11/3}$  power laws and a cutoff frequency of 1 Hz. The closed loop conditions are a 200 Hz sampling frequency, 2 ms time delay, an integrator in the loop. The quantum noise limitation has been assumed. The global optical throughput is 0.3, the quantum efficiency 0.1 on a spectral bandwidth of 400 nm. The telescope diameter is 3.6 m.  $r_0(500 \text{ nm}) = 12 \text{ cm}$

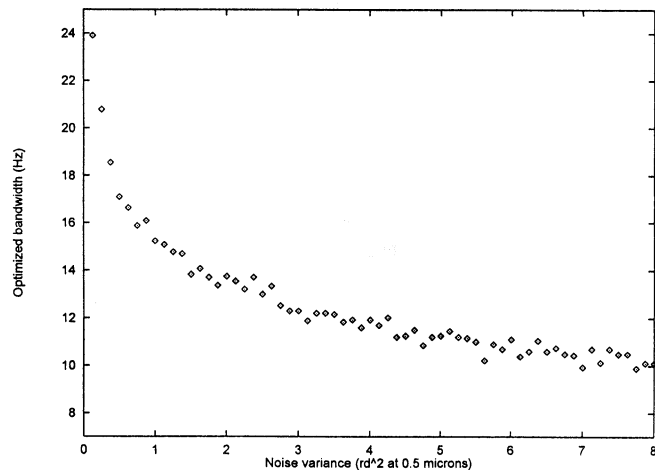


**Fig. 8.** Values of the optimized bandwidth in terms of the noise level. The input turbulence is a simulated spectrum of the astigmatism mode fluctuations, with some  $f^{-2/3}$  and  $f^{-11/3}$  power laws and a cutoff frequency of 1 Hz. The  $r_0(500 \text{ nm})$  is 12 cm, on a 4 m telescope. Units of the noise variance are  $\text{rd}^2$  at 500 nm. The closed loop conditions are a 200 Hz sampling frequency, 2 ms time delay, an integrator in the loop

The test can be repeated keeping the same turbulence spectrum, but taking another random trial of the noise. The noise level is unchanged. The optimum gain is always found to be at the same location with a good accuracy. Moreover the hollow is sufficiently flat and smooth so that the errors on the determination of  $g_i$  have a negligible impact. Figure 7 illustrates the dispersion of the optimized gain values.

The impact of the noise level can now be studied. Figure 8 shows the values of the optimized bandwidth in terms of the noise variance. The turbulence conditions are the same as on Fig. 5, only the noise level is changed, from 0 to 7  $\text{rd}^2$  (at 500 nm).

This section has shown that it is possible to follow the approach described in Sect. 4.3, simply by feeding the equations with some quantities measured with the system before closing the loop. The optimum gain value found with this method is stable and reliable.

## 5. An observer's point of view

The above presentation discussed the optimization in terms of the quantities used in Sect. 3.2. The user of an AO system has a slightly different point of view, as he currently refers to common quantities such as the magnitude of the star, the seeing conditions, the wind velocity, etc. It is appropriate to show at least qualitatively how these parameters impact on the concept of optimization developed in this paper. These parameters are the reference object magnitude  $m_v$ , the  $r_0$  value, the wind velocity, the system sampling frequency and the anisoplanacity. It is assumed here for simplicity that the WFS is working in a photocounting regime in the V band.

### 5.1. The magnitude of the reference object

The magnitude of the reference object used to measure the wavefront is the most influential parameter since it imposes the noise variance. Figure 9 is the same as Fig. 8, but translated in magnitude units. As expected, the optimum bandwidth decreases with the magnitude because of the loss in SNR. For the 60<sup>th</sup> Zernike polynomial ( $n = 10$ ,  $m = 4$ ) the points have to be shifted 2.4 magnitudes towards the left.

### 5.2. The seeing conditions

The seeing conditions are characterized by the FWHM of the distorted image, equal to  $0.97 \frac{\lambda}{r_o}$ . The  $r_o$  variations not only influence the turbulent spectrum shape but also the noise level, since the image width is affected. Assuming the turbulence to be Kolmogorov, the amplitude of the atmospheric fluctuations is proportional to  $r_o^{-5/3}$ . Assuming Eq. (3) to be valid, the noise level is proportional to  $r_o^{-2}$ . The optimum bandwidth only depends on the noise level position with respect to the turbulence, and this varies as  $r_o^{1/3}$ . If the intersection is on the  $-11/3$  slope, the optimum bandwidth will vary proportional to  $r_o^{-1/11}$ . A  $r_o$  variation from 20 cm to 5 cm only makes a variation of 12% on the bandwidth, which is negligible.

In conclusion, the optimized gains are roughly independent of the seeing conditions.

### 5.3. The wind velocity

Modifying the wind velocity changes the mode cutoff frequency. In order to keep the variance of the mode fluctuations constant, the increase of  $f_c$  has to go with a decrease of the global amplitude. On a log-log scale, this displaces the turbulent spectrum along a direction parallel to  $-1$  decade/decade giving an optimum bandwidth proportional to  $f_c^{8/11}$  if the intersection is on the  $-11/3$  slope and  $f_c^{-1/2}$  if on the  $-2/3$  slope. Here things become extremely dependent on the spectrum shape, i.e. on the turbulence spatio-temporal characteristics. This cannot be treated with a model as simple as the one described in this paragraph: the evolution of the wind speed may modify the spectrum shape in various ways. The phase distortion comes from the contributions of different sources: several turbulent layers and dome seeing. Each of them may vary independently of the other, and modify the turbulence structure in a random manner.

### 5.4. The sampling frequency

With a quantum noise limited detector, the noise variance is proportional to the sampling frequency. This implies that this noise level on the mode spectrum is a constant independent of the sampling rate. The turbulence power spectrum is also independent of the sampling rate. Hence the choice of the best sampling rate is only linked to the system properties and not to the outer parameters. This leads us to make use of the maximal sampling frequency since the larger the sampling rate, the easier it will be to achieve the required bandwidth. But a limitation occurs when the number of photocounts per frame is so small that Eq. (3) becomes false: when no photon is received, the centroid of the spot cannot be determined. The noise takes another expression, depending on how the system reacts when no signal is received. As a conclusion, the sampling rate has to be set as high as possible, as soon as the lack of photons does not become a limitation for the system.

It is worth noticing this reasoning becomes false with a read-out noise limited detector: in this case the noise level increases with the sampling frequency.

### 5.5. The problem of isoplanaticity

This paper has ignored the case where the reference object is distinct from the object to be imaged, although this in practice is a useful observing mode. Although it is possible to theoretically derive the effect of this anisoplanatic angle on the  $z'_i$  (Abitbol 1991), the derivation of this effect from actual AO system measurements has not yet been explored. It is therefore not possible to use the same approach as that given in Sect. 3.2, and the issue has been left aside in this paper.

## 6. Conclusion

The concept of modal control is not entirely new in AO theory, but its use as a tool for optimizing the system performance in astronomy on closed loop systems had not been investigated before.

We have demonstrated the need for the optimization: at low flux level, the image quality, characterized by the phase residual error, can be improved by reducing the system correction performance. In particular the temporal correction bandwidth of each mirror mode has to be adjusted. The goal was to derive an optimization method using data and parameters exclusively derived from the AO system itself. No assumption is made on the turbulence structure; everything is measured. Unfortunately, because of this restriction the case of the anisoplanatism problem, although similar, had to be left aside. For simplicity the study has been limited to the case of a Shack-Hartmann type wave-front sensor, but the method can be extended to any linear sensor.

The optimization process has been shown to be reliable, with no convergence problem. An optimized control matrix is computed before closing the loop, without requiring any extra real-time computation when the loop is closed. This leads to a flexible system where the number of degrees of freedom is gradually adjustable in terms of the observing conditions, from a full correction to a simple tilt correction at the limiting magnitude of the instrument.

However, there is no interest to keep on testing the method on simulated data since it is designed to be used on real systems. Simulated data do not properly take into account the effects of the dome seeing or the convection phenomena on the primary mirror. These effects may strongly depart from a Kolmogorov distribution. Fortunately, observations carried in 1992-1993 with the AO system Come-On-Plus provide a wealth of experimental data. They are the basis of a forthcoming paper which will compare the reality with the theoretical predictions made in the present one on the basis of simple assumptions.

*Acknowledgements.* The authors wish particularly to thank G. Rousset and S. Ridgway for helpful discussions, and all the members of the Come-On-Plus team. E. Gendron has been supported by a CIFRE PhD contract kindly provided by Laserdot and ANRT.

## Appendix

Assuming the amplitude of the electric field is constant over the pupil area, the deviation angle  $s$  of the image is derived from the phase gradient by

$$\mathbf{s} = \frac{\lambda}{2\pi} \int_{\text{Aperture}} \nabla \phi \quad (20)$$

Using the theorem of the gradient leads to

$$s = \frac{\lambda}{2\pi S} \int_C \phi(M) \mathbf{n}(M) dl \quad (21)$$

The angle  $s$  is supposed to be measured along a particular direction. The integral is curvilinear along the aperture contour  $C$ ,  $S$  is the aperture area,  $\mathbf{n}(M)$  is the component of the vector normal to the contour at point  $M$  directed along the axis of measurement.

The correlation between the angles of arrival of two subapertures is computed. The subapertures are defined by the subscript  $i$  and  $j$ .

$$\begin{aligned} \langle s_i s_j \rangle &= \frac{\lambda}{4\pi^2 S_i S_j} \\ \int_{C_i} \int_{C_j} \langle \phi(M) \cdot \phi(M') \rangle \mathbf{n}_i(M) \mathbf{n}_j(M) dl dl' \end{aligned} \quad (22)$$

One can write

$$\begin{aligned} \langle \phi(M) \cdot \phi(M') \rangle &= -\frac{1}{2} D_\phi(MM') \\ &+ \frac{\langle \phi^2(M) \rangle}{2} + \frac{\langle \phi^2(M') \rangle}{2} \end{aligned} \quad (23)$$

where  $D_\phi(MM')$  is the phase structure function value, and  $MM'$  stands for the distance between the points  $M$  and  $M'$ . The two last terms are constant and vanish in the curvilinear integral. Equation (22) becomes:

$$\begin{aligned} \langle s_i s_j \rangle &= -\frac{\lambda}{8\pi^2 S_i S_j} \\ \int_{C_i} \int_{C_j} D_\phi(MM') \mathbf{n}_i(M) \mathbf{n}_j(M) dl dl' \end{aligned} \quad (24)$$

## References

- Abitbol M., Ben-Yosef N., 1991, *Waves in random media* 2, 99  
 Acton D.S., Sharbaugh R.J., Roehrig J.R., Tiszauer D., 1992, *Appl. Optics* 31, 4280  
 Babcock H.W., 1953, *PASP* 65, 229  
 Beckers J.M., 1993, *ARA&A* 31  
 Boyer C., Michau V., Rousset G., 1990, *Proc. SPIE* 1237, 406  
 Chassat F., 1989, *J. Optics (Paris)* 20, 13  
 Clifford S.F., 1971, *JOSA* 61, 1285  
 Fields D.R., 1983, *Appl. Opt.* 22, 645  
 Fried D.L., 1977, *JOSA* 67, 370  
 Fugate R.Q., Fried D.L., Ameer G.A., 1991, *Nature* 353, 144  
 Fugate R.Q., 1992, In: Ulrich M.-H. (eds.) *ESO Conf. on Progress in Telescope and Instrumentation Technologies*, 407

- Gaffard J.P., Ledanois G., 1991, *Proc. SPIE* 1542, 34  
 Gendron E., 1993, In: F. Merkle (eds.) *ICO Conf. on Active and Adaptive Optics*, 187  
 Greenwood D.P., Fried D.L., 1976, *JOSA* 66, 193  
 Greenwood D.P., 1978, *Proc. SPIE* 142, 91  
 Greenwood D.P., Primmerman C.A., Murphy D.G., 1988, In: Ulrich M.-H. (eds.) *ESO Conf. on Very Large Telescopes and their Instrumentation*, 675  
 Hermann J., 1981, *JOSA* 71, 989  
 Hogge C.B., Butts R.R., 1976, *IEEE transaction on antennas and propagation* 24 No 2, 114  
 Hubin N., Noethe L., 1993, *Science* 262, 1390  
 Léna P., 1990, *Optique adaptative et VLT*, In: Alloin D., Léna P. (eds.) *Forum de l'Observatoire de Paris*, 1  
 Léna P., 1994a, *Proc. SPIE* 2201  
 Léna P., 1994b, In: Alloin D., J.-M. Mariotti (eds.) *Adaptive optics for astronomy*, NATO-ASI, Kluwer, 321  
 Madec P.-Y., Conan J.-M., Rousset G., 1992, In: Ulrich M.-H. (eds.) *ESO Conf. on Progress in Telescope and Instrumentation Technologies*, 471  
 Noll R.J., 1976, *JOSA* 66, 207  
 Primmerman C.A., Murphy D.G., Page D.A., Zollars B.G., Barclay H.T., 1991, *Nature* 353, 141  
 Rigaut F., Gendron E., 1992, *A&A* 261, 678  
 Roddier F., 1981, In: Wolf E. (eds.) *Progress in Optics Vol. XIX*, 283  
 Roddier F., Northcott M., Graves J.E., 1991, *PASP* 103, 131  
 Roddier F., Northcott M., Graves J.E., McKenna D.L., 1993, *JOSA* 10 No. 5, 957  
 Roddier N., 1990, *Proc. SPIE* 1237  
 Rousset G., Primot J., Fontanella J.C., 1987, *Proc. LEST on Adaptive Optics in Solar Observations*, 17  
 Rousset G., Beuzit J.-L., Hubin N. et al., 1993, In: Merkle F. (eds.) *ICO Conf. on Active and Adaptive Optics*, 65  
 Southwell W.H., 1980, *JOSA* 70, 998  
 Southwell W.H., 1982, *Proc. SPIE* 365, 97  
 Wallner E.P., 1983, *JOSA* 73, 12  
 Wang J.Y., Markey J.K., 1978, *JOSA* 68, 78

This article was processed by the author using Springer-Verlag L<sup>A</sup>T<sub>E</sub>X A&A style file version 3.